DIGITAL SIGNAL PROCESSING 6, 108–125 (1996)
ARTICLE NO. 0011

# Comparison between the Matrix Pencil Method and the Fourier Transform Technique for High-Resolution Spectral Estimation

José Enrique Fernández del Río and Tapan K. Sarkar*

Department of Electrical and Computer Engineering, 121 Link Hall,
Syracuse University, Syracuse, New York 13244-1240

Fernández del Río, J. E., and Sarkar, T. K., Comparison between the Matrix Pencil Method and the Fourier Transform Technique for High-Resolution Spectral Estimation, *Digital Signal Processing* 6 (1996), 108–125.

The objective of this paper is to compare the performance of the Matrix Pencil Method, particularly the Total Forward–Backward Matrix Pencil Method, and the Fourier Transform Technique for high-resolution spectral estimation. Performance of each of the techniques, in terms of bias and variance, in the presence of noise is studied and the results are compared to those of the Cramer–Rao Bound. © 1996 Academic Press, Inc.

## 1. INTRODUCTION

In this work, the Total Forward–Backward Matrix Pencil Method (TFBMPM) is utilized for the high-resolution estimator and its results are compared with those of the Fourier Transform Technique, which is a straightforward implementation of the Fourier Transform. The root mean squared error for both of the methods is also considered in making a comparison in performance.

Simulation results are presented to illustrate the performance of each of the techniques.

## 2. SIGNAL MODEL

Consider a time domain signal of the form

$$g(t) = \sum_{m=1}^{K} A_m e^{j2\pi f_m t}, \tag{2.1}$$

* Fax: (315) 443-4441. E-mail: tksarkar@mailbox.syr.edu.

where $j$ is $\sqrt{-1}$, $K$ is the number of frequency components, and $A_m$ is the complex amplitude at frequency $f_m$.

The time function is sampled at $N$ equispaced points, $\Delta t$ apart. Hence (2.1) reduces to

$$g(i\Delta t) = \sum_{m=1}^{K} A_m e^{j2\pi f_m i\Delta t}; \quad i = 0, \ldots, N-1. \tag{2.2}$$

The signal in (2.2) may be contaminated by noise to produce $z(i\Delta t)$. The additive white noise $w(i\Delta t)$ is assumed to be Gaussian with zero mean and variance $2\sigma^2$, and it is included in our model via

$$z(i\Delta t) = g(i\Delta t) + w(i\Delta t); \quad i = 0, \ldots, N-1. \tag{2.3}$$

In order to simplify the notation, Eq. (2.3) will be rewritten as

$$z_i = g_i + w_i; \quad i = 0, \ldots, N-1. \tag{2.4}$$

The frequency estimation problem consists of estimating $K$ frequency components from a known set of noise contaminated observations, $z_i$, $i = 0, \ldots, N-1$.

In this paper, the frequency estimation problem will be solved by using an extension of the Matrix Pencil Method (MPM) [1] called Total Forward–Backward Matrix Pencil Method and compared with the results obtained from the Fourier Techniques.

1051-2004/96 $18.00
Copyright © 1996 by Academic Press, Inc.
All rights of reproduction in any form reserved.

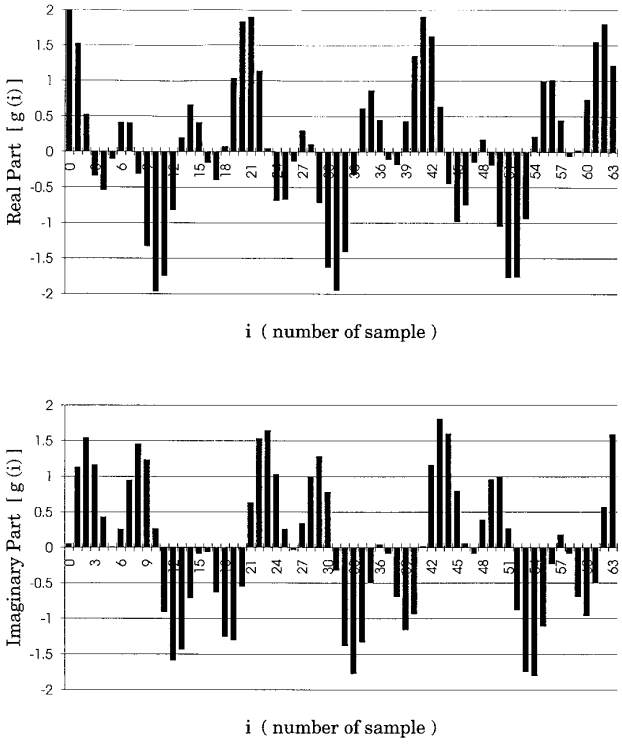


FIG. 1. Real and imaginary parts of an undamped cisoid formed by two frequency components of equal power.

In Fig. 1, a possible noiseless data record (real and imaginary part of the signal) is shown. The function represented was generated using Eq. (2.2) with the parameters given in Table 1.

This function will be utilized in making a comparison between the Matrix Pencil Method and the Fourier Transform Technique.

## 3. TOTAL FORWARD–BACKWARD MATRIX PENCIL METHOD

The estimation of frequencies in the presence of noise is considered by the TFBMPM. When the complex exponentials in (2.2) (so-called cisoids) are undamped[1] (which is the case in this work), to improve the estimation accuracy we consider the matrices $Z_{0fb}$ and $Z_{1fb}$ as defined by

$$Z_{0fb_{2(N-L)\times L}} = \begin{bmatrix} z_0 & z_1 & \cdots & z_{L-1} & z_{L-1} \\ z_L^* & z_{L-1}^* & \cdots & z_2^* & z_1^* \end{bmatrix} \quad (3.1)$$

[1] Note that the Matrix Pencil Method can solve a more general problem [1], the pole estimation, $p_m$, for damped cisoids ($p_m = e^{(-s_m + j\omega_m)\Delta t}$, $s_m \geqslant 0$, $m = 1, \ldots, K$) and the undamped cisoids are a particular case of the damped exponentials (in that it is enough to set $s_m$ to zero for all $m$).

$$Z_{1fb_{2(N-L)\times L}} = \begin{bmatrix} z_1 & z_2 & \cdots & z_{L-1} & z_L \\ z_{L-1}^* & z_{L-2}^* & \cdots & z_1^* & z_0^* \end{bmatrix}, \quad (3.2)$$

where * denotes complex conjugate, $L$ is called the pencil parameter, and the transpose of $z_j$ ($j = 0, \ldots, L$) is defined as

$$z_j^T = [z_j, z_{j+1}, \ldots, z_{N-L+j-1}]; \quad j = 0, \ldots, L. \quad (3.3)$$

The new $Z_{0fb}$ and $Z_{1fb}$ are better conditioned [2, Appendix B] than $Z_0$ and $Z_1$, which are formed for the ordinary MPM; that is, $Z_{0fb}$ and $Z_{1fb}$ are less sensitive than $Z_0$ and $Z_1$ to small changes in the element values.

With (3.1) and (3.2) one can build the Matrix Pencil, $Z_{1fb} - \xi Z_{0fb}$ ($\xi$ is a complex scalar), and follow the method proposed in [1, Section II] to estimate the frequency components, but, for noisy data, the best strategy is to perform a Singular Value Decomposition (SVD) [3] on the "all data" matrix [4]. This matrix is given by

$$Z_{fb_{2(N-L)\times(L+1)}} = \begin{bmatrix} z_0 & z_1 & \cdots & z_{L-1} & z_L \\ z_L^* & z_{L-1}^* & \cdots & z_1^* & z_0^* \end{bmatrix}. \quad (3.4)$$

It is easy to see that $Z_{fb}$ contains both $Z_{0fb}$ and $Z_{1fb}$:

$$Z_{fb_{2(N-L)\times(L+1)}} = [Z_{0fb_{2(N-L)\times L}}, c_{L+1}] \quad (3.5)$$

$$Z_{fb_{2(N-L)\times(L+1)}} = [c_1, Z_{1fb_{2(N-L)\times L}}]; \quad (3.6)$$

here $c_1$ and $c_{L+1}$ represent, respectively, the first and $(L+1)$th columns of $Z_{fb}$.

On the other hand, the SVD of $Z_{fb}$ is

$$Z_{fb_{2(N-L)\times(L+1)}} = U_{2(N-L)\times 2(N-L)} \Sigma_{2(N-L)\times(L+1)} V^H_{(L+1)\times(L+1)}, \quad (3.7)$$

TABLE 1

Input Data Considered in Fig. 1

64 samples ($N = 64$)
Sampling period 0.25 ms ($\Delta t = 1/4000$ s)

2 frequency components ($K = 2$)
$A_1 = 1e^{j2.7(\pi/180)}$
$A_2 = 1\ e^{j0}$
$f_1 = 580$ Hz
$f_2 = 200$ Hz

where the superscript $H$ denotes complex conjugate transpose of a matrix and $U$, $\Sigma$, and $V$ are given by

$$\Sigma = \text{diag}\{\sigma_1, \sigma_2, \ldots, \sigma_p\};$$

$$p = \min\{2(N-L), L+1\} \tag{3.8}$$

$$\sigma_1 \geqslant \sigma_2 \geqslant \cdots \geqslant \sigma_p \geqslant 0 \tag{3.9}$$

$$U = [\mathrm{u}_1, \mathrm{u}_2, \ldots, \mathrm{u}_{2(N-L)}];$$

$$Z_{fb}^H \mathrm{u}_i = \sigma_i \mathrm{v}_i, \; i = 1, \ldots, p \tag{3.10}$$

$$V = [\mathrm{v}_1, \mathrm{v}_2, \ldots, \mathrm{v}_{L+1}];$$

$$Z_{fb}\mathrm{v}_i = \sigma_i \mathrm{u}_i, \quad i = 1, \ldots, p \tag{3.11}$$

$$U^H U = I, \quad V^H V = I. \tag{3.12}$$

$\sigma_i$ are the singular values of $Z_{fb}$ and the vectors $\mathrm{u}_i$ and $\mathrm{v}_i$ are, respectively, the $i$th left singular vector and the $i$th right singular vector.

The problem can be computationally improved by applying the singular value filtering, which consists of [1] using the $K$ largest singular values of $Z_{fb}$, i.e.,

$$\hat{Z}_{fb_{2(N-L)\times(L+1)}} = \hat{U}_{2(N-L)\times K}\hat{\Sigma}_{K\times K}\hat{V}^H_{K\times(L+1)}, \tag{3.13}$$

where

$$\hat{\Sigma} = \text{diag}\{\sigma_1, \sigma_2, \ldots, \sigma_K\} \tag{3.14}$$

has the $K$ largest singular values of $\Sigma$ and the columns of $\hat{U}$ and $\hat{V}$ are formed by extracting the singular vectors corresponding to those $K$ singular values.

Eq. (3.13) can be rewritten as

$$\hat{Z}_{fb} = \hat{U}\hat{\Sigma}\hat{V}^H = \hat{U}\hat{\Sigma}[\mathrm{t}_1, \mathrm{t}_2, \ldots, \mathrm{t}_{L+1}]$$
$$= [\hat{U}\hat{\Sigma}\mathrm{t}_1 | \hat{U}\hat{\Sigma}\mathrm{t}_2 \cdots \hat{U}\hat{\Sigma}\mathrm{t}_L | \hat{U}\hat{\Sigma}\mathrm{t}_{L+1}]. \tag{3.15}$$

Comparing (3.5), (3.6), and (3.15), the equations

$$\hat{Z}_{0fb} = \hat{U}\hat{\Sigma}\hat{V}^H_0 \tag{3.16}$$

$$\hat{Z}_{1fb} = \hat{U}\hat{\Sigma}\hat{V}^H_1 \tag{3.17}$$

can be established, where $\hat{V}_0$ and $\hat{V}_1$ are obtained from $\hat{V}$, deleting, respectively, its $(L+1)$th and first columns, i.e.,

$$\hat{V} = [\hat{V}_0, \mathrm{v}_{L+1}], \quad \hat{V} = [\mathrm{v}_1, \hat{V}_1]. \tag{3.18}$$

By considering the matrix pencil

$$\hat{Z}_{1fb} - \xi\hat{Z}_{0fb} \tag{3.19}$$

and right multiplying (3.19) by $\hat{Z}^+_{0fb}$, the resulting eigenproblem can be expressed as

$$\mathrm{q}^H(\hat{Z}_{1fb}\hat{Z}^+_{0fb} - \xi I) = 0^H, \tag{3.20}$$

where $\hat{Z}^+_{0fb}$ is the Moore–Penrose pseudoinverse [3] of $\hat{Z}_{0fb}$ and it can be written as

$$\hat{Z}^+_{0fb} = (\hat{V}^H_0)^+\hat{\Sigma}^{-1}\hat{U}^+. \tag{3.21}$$

Substituting (3.17) and (3.21) into (3.20), the equivalent generalized eigen-problem becomes

$$\mathrm{q}^H(\hat{V}^H_1 - \xi\hat{V}^H_0) = 0^H. \tag{3.22}$$

It can be shown that (3.22) is equivalent to

$$\mathrm{q}^H(\hat{V}^H_1\hat{V}_0 - \xi\hat{V}^H_0\hat{V}_0) = 0^H, \tag{3.23}$$

which is a generalized eigenproblem of dimension $K \times K$.

Using the values of the generalized eigenvalues, $\xi$, of (3.23), the frequency components can be estimated.

In the following, the *algorithm* applied to estimate the frequencies is summarized as:

*Step 1:* Construct the matrix $Z_{fb}$, (3.4), with the corrupted samples, where $\mathrm{z}_j^T$ $(j = 0, \ldots, L)$ is defined as in (3.3), and $L$ has to satisfy

$$K \leqslant L \leqslant N - K. \tag{3.24}$$

*Step 2:* Realize the SVD of $Z_{fb}$, (3.7), and, from its singular values, estimate $K$ (number of frequency components). This problem is equivalent to solving the eigenproblem $Z^H_{fb}Z_{fb}$; i.e., it can be proved that the singular values of $Z_{fb}$, $\sigma_i$, are the nonnegative square roots of $\eta_i$, where $\eta_i$ are the eigenvalues of the eigenproblem

$$(Z^H_{fb}Z_{fb} - \eta_i I)\mathrm{r}_i = 0. \tag{3.25}$$

*Step 3:* Extract $\hat{V}_0$ and $\hat{V}_1$ from $\hat{V}$, (3.18), where $\hat{V}$ is the $K$-truncation of $V$ ((3.7) to (3.14)).

*Step 4:* Estimate the $K$ frequencies using the $K$ generalized eigenvalues, $\xi_m$, of (3.23), such that those eigenvalues can be expressed as

$$\xi_m = \text{Real}(\xi_m) + j\,\text{Imag}(\xi_m);$$
$$m = 1, \ldots, K, \tag{3.26}$$

where $\text{Real}(\xi_m)$ and $\text{Imag}(\xi_m)$ are, respectively, the

real and imaginary parts of $\xi_m$, but those eigenvalues are related to the frequencies as

$$\xi_m \approx e^{j2\pi f_m \Delta t}; \quad m = 1, \ldots, K. \tag{3.27}$$

And, from (3.26) and (3.27),

$$f_m \approx \frac{1}{2\pi\Delta t} \tan^{-1}\left(\frac{\text{Imag}(\xi_m)}{\text{Real}(\xi_m)}\right); \quad m = 1, \ldots, K. \tag{3.28}$$

## 4. LIMITS OF TFBMPM FOR FREQUENCIES ESTIMATION

### *4.1. The Frequency Estimation Problem*

The frequency estimation problem consists of [5, Chapter 6] determining the frequency components of a signal, which obeys the mathematical model of Section 2, from a set of noisy samples.

Any estimate of the frequency parameter evaluated from a set of samples involves a random process and, thus, it is necessary to consider the estimate as a random variable. Consequently, it is not correct to speak of a particular value of an estimate, but it is necessary to know its statistical distribution if the accuracy of the estimate is analyzed.

An efficient estimate has to be as near as possible to the true value of the parameter to be estimated [6, Chapter 32]. This idea of "concentration" or "dispersion" about the true value may be measured using several statistical magnitudes (variance, mean squared error, etc.).

One of the first works concerned with the application of the Estimation Theory by Fisher and Cramer to the problem of estimating signal parameters is that of Slepian [7]; later, in [8], the statistical theory is applied to the estimation of the Direction of Arrival of a plane wave impinging on a linear phased array.

In this work, the limits of TFBMPM for frequency estimation will be pointed out and the variance of this method will be compared with that of the Cramer–Rao Bound (CRB) [6, Chapter 32].

### *4.2. The Cramer–Rao Bound*

In this section, the notation

$$g_i = \sum_{m=1}^{K} |A_m| e^{j\theta_m} e^{j\omega_m i\Delta t}; \quad i = 0, \ldots, N-1, \tag{4.2.1}$$

has been followed, where

$$A_m = |A_m| e^{j\theta_m}; \quad m = 1, \ldots, K \tag{4.2.2}$$

$$\omega_m = 2\pi f_m; \quad m = 1, \ldots, K. \tag{4.2.3}$$

For the noisy data problem it is enough to consider (2.4), which, in vectorial notation, can be denoted as

$$\mathrm{z} = \mathrm{g} + \mathrm{w}, \tag{4.2.4}$$

where

$$\mathrm{z}^T = [z_0, z_1, \ldots, z_{N-1}] \tag{4.2.5}$$

$$\mathrm{g}^T = [g_0, g_1, \ldots, g_{N-1}] \tag{4.2.6}$$

$$\mathrm{w}^T = [w_0, w_1, \ldots, w_{N-1}] \tag{4.2.7}$$

and those vectors could be briefly described as follows:

g is formed by the noise free samples, (4.2.1). This vector may be seen like a deterministic unknown magnitude. The deterministic model for g is used when $K$ (number of frequency components) and the number of snapshots (in this work just one snapshot or "picture" is considered) are small [9].

w represents the complex white Gaussian noise, with the characteristics

$$\text{zero mean:} \quad E[\mathrm{w}] = 0 \tag{4.2.8}$$

uncorrelated, with variance $2\sigma^2$:

$$R_{\mathrm{w}} = 2\sigma^2 I_{N\times N}, \tag{4.2.9}$$

where $E[\cdot]$ means expected value, $R_{\mathrm{w}}$ is the correlation matrix of the noise, and $I_{N\times N}$ is the identity matrix.

z is the vector containing the observed data. Obviously, from its definition, (4.2.4), it is a random vector.

In order to define the CRB it is first necessary to introduce the joint probability density function (jpdf). The jpdf of a complex Gaussian random vector of $N$ components, x, is defined [5, p. 478] as

$$f_{\mathrm{x}}(\mathrm{x}) = \frac{1}{\pi^N \det(R_{\mathrm{x}})} e^{-(\mathrm{x}-E[\mathrm{x}])^H R_{\mathrm{x}}^{-1}(\mathrm{x}-E[\mathrm{x}])}, \tag{4.2.10}$$

where $\det(\cdot)$ means determinant of a matrix, $H$ de-

notes complex conjugate transpose, and $-1$ indicates the inverse of a matrix.

Therefore, the jpdf of w can be evaluated by using (4.2.8)–(4.2.10):

$$f_{\mathrm{w}}(\mathrm{w}) = \frac{1}{(2\pi\sigma^2)^N}\, e^{-1/2\sigma^2 \sum_{i=0}^{N-1} |w_i|^2}. \quad (4.2.11)$$

The jpdf of z can be obtained from (4.2.11) by taking into account the relationship [10, p. 61] between z and w, which is given by (4.2.4),

$$f_{\mathrm{z}|\boldsymbol{\alpha}}(\mathrm{z}|\boldsymbol{\alpha}) = \frac{1}{(2\pi\sigma^2)^N}\, e^{-1/2\sigma^2 \sum_{i=0}^{N-1} |z_i - g_i|^2}, \quad (4.2.12)$$

where $|\boldsymbol{\alpha}$ denotes that the jpdf is conditioned to an unknown vector parameter, $\boldsymbol{\alpha}$, and $g_i$ is given in (4.2.1).

From (4.2.12) one can deduce that z is a Gaussian random vector with

$$E[\mathrm{z}] = \mathrm{g} \quad (4.2.13)$$

$$R_{\mathrm{z}} = 2\sigma^2 I_{N\times N}. \quad (4.2.14)$$

Also, $\boldsymbol{\alpha}$ is the vector formed by the parameters to be estimated. In this work the complex amplitudes of the signals, $A_m$,[2] and the variable $\omega_m$ in (4.2.1) will be chosen as unknown parameters. Note that $A_m$ is given by (4.2.2) and, therefore, each $A_m$ corresponds to two parameters, $|A_m|$ and $\theta_m$. On the other hand, $\omega_m$ is related to the frequencies through (4.2.3).

Consequently, the vector $\boldsymbol{\alpha}$ can be written as

$$\boldsymbol{\alpha}^T = [\alpha_1, \alpha_2, \alpha_3, \ldots, \alpha_{3K-2}, \alpha_{3K-1}, \alpha_{3K}], \quad (4.2.15)$$

where

$$\alpha_{3m-2} = \omega_m = 2\pi f_m; \quad \alpha_{3m-1} = |A_m|;$$
$$\alpha_{3m} = \theta_m; \quad m = 1, \ldots, K. \quad (4.2.16)$$

The CRB provides the goodness of any estimate of a random parameter. The estimates of this work have been computed via the TFBMPM, and it will be pointed out, through simulation results, that they are almost unbiased[3] in the region where the TFBMPM works.

For unbiased estimates, the CRB states that if $\hat{\alpha}$ is an unbiased estimate of $\boldsymbol{\alpha}$, the variance of each element, $\hat{\alpha}_l$ ($l = 1, \ldots, 3K$), of $\hat{\alpha}$ can be no smaller than the corresponding diagonal term in the inverse of the Fisher Information Matrix

$$\mathrm{var}(\hat{\alpha}_l) \geqslant [F^{-1}]_{ll}, \quad (4.2.17)$$

where $\hat{\alpha}_l$ is the estimate of the parameter $\alpha_l$ ($l = 1, \ldots, 3K$), $[F^{-1}]_{ll}$ is the $l$th diagonal element of the inverse of $F$, and $F_{3K\times 3K}$ is the Fisher Information Matrix.

The $(m, n)$th element of $F$ is defined as

$$[F]_{mn} = E\left[\frac{\partial \ln f_{\mathrm{z}|\boldsymbol{\alpha}}(\mathrm{z}|\boldsymbol{\alpha})}{\partial\alpha_m} \cdot \frac{\partial \ln f_{\mathrm{z}|\boldsymbol{\alpha}}(\mathrm{z}|\boldsymbol{\alpha})}{\partial\alpha_n}\right];$$
$$m, n = 1, \ldots, 3K. \quad (4.2.18)$$

The last equation, using (4.2.12), can be rewritten [1] as

$$[F]_{mn} = \frac{1}{2\sigma^2} \sum_{i=0}^{N-1} 2\ \mathrm{Real}\left[\frac{\partial g_i}{\partial\alpha_m} \cdot \frac{\partial g_i^*}{\partial\alpha_n}\right];$$
$$m, n = 1, \ldots, 3K, \quad (4.2.19)$$

where Real[$\cdot$] denotes the real part.

It can be proved [11] that $F^{-1}$ may be decomposed as

$$F^{-1}_{3K\times 3K} = \sigma^2 S_{3K\times 3K} P^{-1}_{3K\times 3K} S_{3K\times 3K}, \quad (4.2.20)$$

where

$$S_{3K\times 3K} = \mathrm{diag}\{[S_1]_{3\times 3}, [S_2]_{3\times 3}, \ldots, [S_K]_{3\times 3}\} \quad (4.2.21)$$

$$[S_m]_{3\times 3} = \mathrm{diag}\{|A_m|^{-1}, 1, |A_m|^{-1}\}; \quad m = 1, \ldots, K \quad (4.2.22)$$

$$P_{3K\times 3K} = \begin{bmatrix} [P_{11}]_{3\times 3} & \cdots & [P_{1K}]_{3\times 3} \\ \vdots & \ddots & \vdots \\ [P_{K1}]_{3\times 3} & \cdots & [P_{KK}]_{3\times 3} \end{bmatrix} \quad (4.2.23)$$

[2] In order to estimate the complex amplitudes, $A_m$, using the results obtained from the TFBMPM for the frequency components, one may solve a least-squares problem $\mathrm{z} \approx E\mathrm{a}$, where z are the corrupted samples, a contains the complex amplitudes $A_m$, and $E$ is the matrix which applied to a gives g.

[3] An estimate $\hat{\alpha}$ of the vector parameter $\boldsymbol{\alpha}$ is unbiased if $E[\hat{\alpha}] = \boldsymbol{\alpha}$.

$$P_{mn} = \begin{bmatrix} (\Delta t)^2 \sum_{i=0}^{N-1} i^2 \cos \Delta(i, m, n) & -\Delta t \sum_{i=0}^{N-1} i \sin \Delta(i, m, n) & \Delta t \sum_{i=0}^{N-1} i \cos \Delta(i, m, n) \\ \Delta t \sum_{i=0}^{N-1} i \sin \Delta(i, m, n) & \sum_{i=0}^{N-1} \cos \Delta(i, m, n) & \sum_{i=0}^{N-1} \sin \Delta(i, m, n) \\ \Delta t \sum_{i=0}^{N-1} i \cos \Delta(i, m, n) & -\sum_{i=0}^{N-1} \sin \Delta(i, m, n) & \sum_{i=0}^{N-1} \cos \Delta(i, m, n) \end{bmatrix} \quad (4.2.24)$$

$$\Delta(i, m, n) = i(\omega_m - \omega_n)\Delta t + \theta_m - \theta_n;$$
$$i = 0, \ldots, N-1; \quad m, n = 1, \ldots, K. \quad (4.2.25)$$

### 4.3. Simulation Results

*4.3.1. Input Data.* In this section several graphs are presented and discussed in order to facilitate a better understanding of the TFBMPM and its estimation limits.

The methodology followed to obtain the different plots has been to generate a set of $N$ complex samples, using ((4.2.1) to (4.2.4)) and then to apply the TFBMPM as proposed in the algorithm of Section 3. This algorithm was iterated several times when the variance of the frequency estimate was numerically computed.

The input data may be described as follows:

(1) *Observation interval*

8 samples have been considered ($N = 8$).

The sampling period was normalized ($\Delta t = 1$ s).

(2) *Description of the signal*

2 frequency components have been chosen ($K = 2$).

$|A_1| = |A_2| = 1$: Two components of equal power.

$\theta_1$, $\theta_2$: A deterministic model has been assumed for the phases of the frequency components. The difference $\theta_1 - \theta_2$ is taken from values in [0°, 180°). TFBMPM performance depending on $\theta_1 - \theta_2$ is shown in the next section.

$f_1 = 0.200$ Hz.

$f_2$: The second frequency varies between 0.270 and 0.290 Hz and, therefore, the value of $\Delta f$ studied is in the interval [0.070 Hz, 0.090 Hz], where $\Delta f = f_2 - f_1$.

(3) *Statistical considerations for the noise (see Section 4.2)*

The noise was generated by using ISML [12] FORTRAN subroutine GGNML. This subroutine is a Gaussian (0, 1) pseudo-random number generator. With GGNML two sets of $N$ real numbers, $r_{1i}$ and $r_{2i}$ ($i = 0, \ldots, N-1$), are obtained to construct the complex sequence

$$\chi_i = r_{1i} + j r_{2i}; \quad i = 0, \ldots, N-1. \quad (4.3.1.1)$$

Taking into account that the variance of the complex noise, $w_i$, was defined as $2\sigma^2$, it is easy to deduce the relationship

$$w_i = \sqrt{2\sigma^2}\chi_i; \quad i = 0, \ldots, N-1. \quad (4.3.1.2)$$

The SNR, for each frequency component, has been defined as

$$\mathrm{SNR}_m = 10 \log_{10} \frac{|A_m|^2}{2\sigma^2};$$
$$m = 1, \ldots, K. \quad (4.3.1.3)$$

(4) *TFBMPM remarks (see Section 3)*

The first step in the TFBMPM consists of choosing a value for the pencil parameter, $L$, in order to form the $Z_{fb}$ matrix.

The best choice for $L$ is [2]

$$\frac{N}{3} \leqslant L \leqslant \frac{2N}{3}, \quad (4.3.1.4)$$

but, at the same time, $L$ has to satisfy (3.24).

To numerically compute the variance of the frequencies the algorithm proposed in Section 3 has been iterated 500 times (trials). For each trial, a different vector w was randomly taken.

*4.3.2. Performance of the TFBMPM as a function of $\theta_1 - \theta_2$.* The accuracy in the frequencies estimation, using the TFBMPM, depends strongly on the difference of phases between the components of the signal. It has been proved [2] that the inverse of the variance of the frequencies estimates,

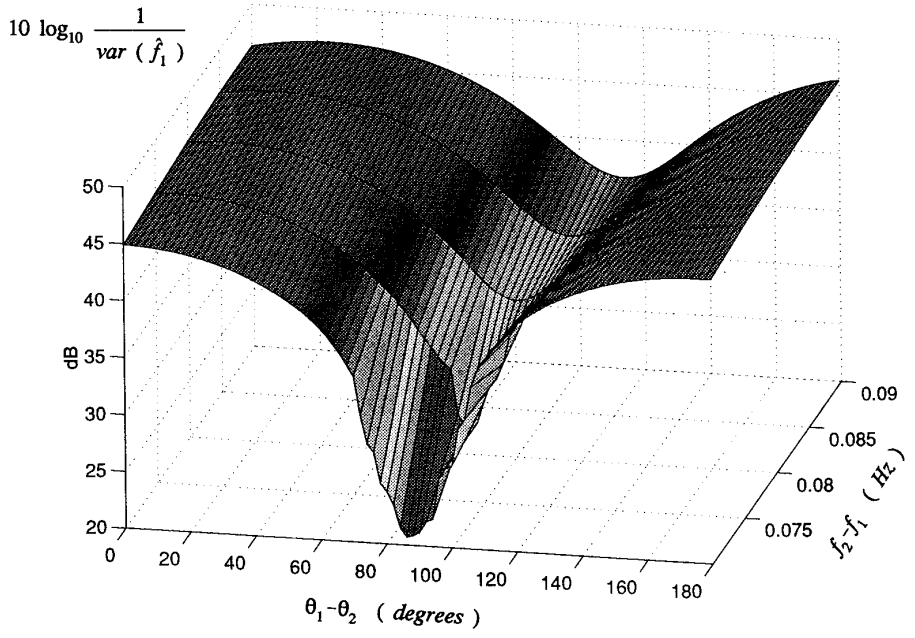


FIG. 2. Inverse of the variance of the first frequency estimate, as a function of the difference of phases of the two frequency components and the difference of frequencies. SNR = 17 dB and the pencil parameter for the TFBMPM is $L = 5$.

$$10 \log_{10} \frac{1}{\mathrm{var}(\hat{f}_m)}; \quad m = 1, \ldots, K, \quad (4.3.2.1)$$

reaches a maximum if

$$(\omega_m - \omega_n)(N-1)\Delta t + 2(\theta_m - \theta_n) = (2l)\pi \quad (4.3.2.2)$$

and a minimum if

$$(\omega_m - \omega_n)(N-1)\Delta t + 2(\theta_m - \theta_n) = l\pi. \quad (4.3.2.3)$$

In both Eqs. (4.3.2.2) and (4.3.2.3), $m$, $n$, and $l$ have to satisfy

$$\text{for all } m \neq n; \quad m, n = 1, \ldots, K; \quad l \text{ integer}. \quad (4.3.2.4)$$

We will call, respectively, best case and worst case to (4.3.2.2) and (4.3.2.3). The meaning is simple; when (4.3.2.2) is given, (4.3.2.1) reaches a maximum and thus the variance takes its minimum value. In other words, the distribution of the estimates reaches its maximum of concentration around the true value of the vector parameter being estimated. The explanation for the worst case is analogous.

In Fig. 2 that dependence is shown. The input data have been explained in Section 4.3.1. SNR is 17 dB and $L = 5$. In Fig. 3 the same input data are taken, and the CRB for the variance of $\hat{f}_1$ is shown. To obtain this 3D plot, the method in Section 4.2 has been followed, determining the CRB for the variance of $\hat{\omega}_1$ and applying the relationship in (4.2.3) to calculate the CRB for $\hat{f}_1$.

Comparing Fig. 2 to Fig. 3 one can deduce that the CRB is reached by the estimate obtained using TFBMPM when $f_2 - f_1$ is close to 0.090 Hz or, in the entire interval [0.070 Hz, 0.090 Hz], when $\theta_1 - \theta_2$ is far from the worst case.

*4.3.3. Estimating the number of frequency components from the singular values of $Z_{fb}$.* As was explained in Section 3, to estimate the number of frequency components $K$ the eigenvalues of $Z_{fb}^H Z_{fb}$ will be used. This idea will be followed in this section for both the ideal sampling (neglecting the noise) and the corrupted samples.

Figures 4 to 11 show the normalized magnitude, in dB, of the eigenvalues, $\xi_n$ ($n = 1, \ldots, L+1$), of $Z_{fb}^H Z_{fb}$. This normalized magnitude is given by

$$10 \log_{10} \frac{\xi_n}{\xi_{\max}}; \quad n = 1, \ldots, L+1, \quad (4.3.3.1)$$

where $L$ is the pencil parameter and $\xi_{\max}$ is the largest eigenvalue.

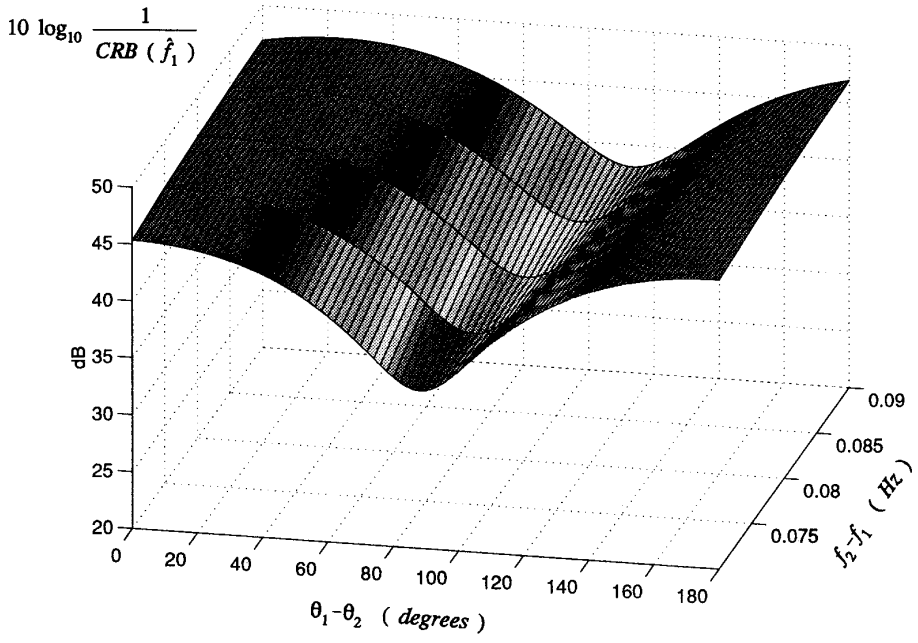


FIG. 3. Inverse of the CRB of the first frequency estimate, as a function of the difference of phases of the two frequency components and the difference of frequencies. SNR = 17 dB.

The input data for SNR, $L$, $f_2 - f_1$, and $\theta_1 - \theta_2$ are given in Table 2.

Comparing the noiseless case (Figs. 4 to 7) to the corrupted samples (Figs. 8 to 11) one can see that the main difference is the "gap" between the second eigenvalue and the third one (note that two frequency components are being considered and the number of signals is estimated from the $K$ largest eigenvalues of $Z_{fb}^{H} Z_{fb}$). This gap is much greater for the noiseless samples than for the samples in noise, as was expected. In fact, the noise is the "culprit" of the gap reduction.

To enhance this gap, for the noisy data case, digital filtering techniques in the original set of samples, $z_i$, can be applied [13].

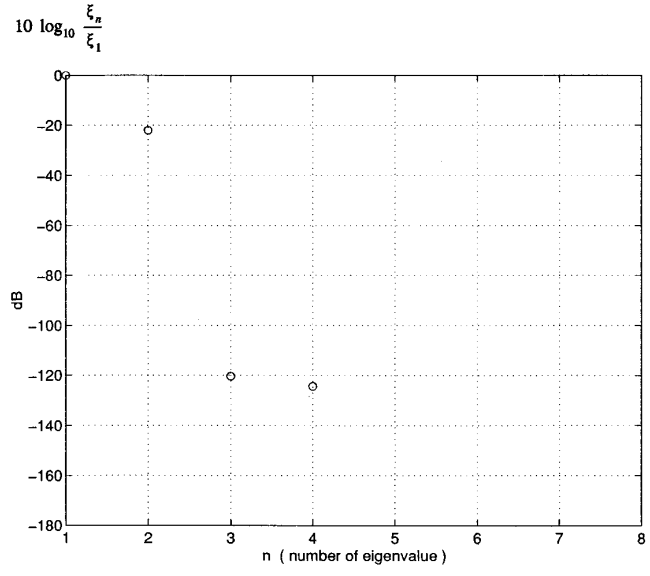


FIG. 4. Normalized magnitude of the eigenvalues of $Z_{fb}^{H} Z_{fb}$. Input data: $N = 8$, $K = 2$, $|A_1| = |A_2| = 1$, $\theta_1 - \theta_2 = 88.2°$ (worst case), $f_2 = 0.270$ Hz, $f_1 = 0.200$ Hz, SNR = $\infty$ (noiseless), $L = 3$.

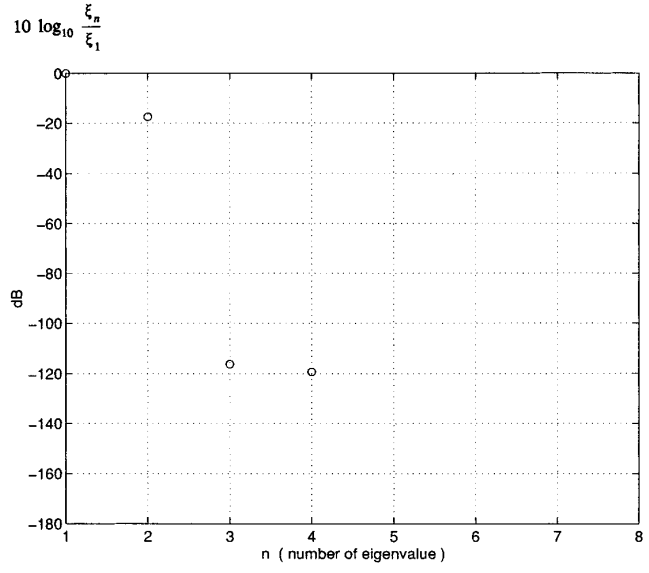


FIG. 5. Normalized magnitude of the eigenvalues of $Z_{fb}^{H} Z_{fb}$. The same input data as in Fig. 4, but $\theta_1 - \theta_2 = 113.4°$ (worst case) and $f_2 = 0.290$ Hz.

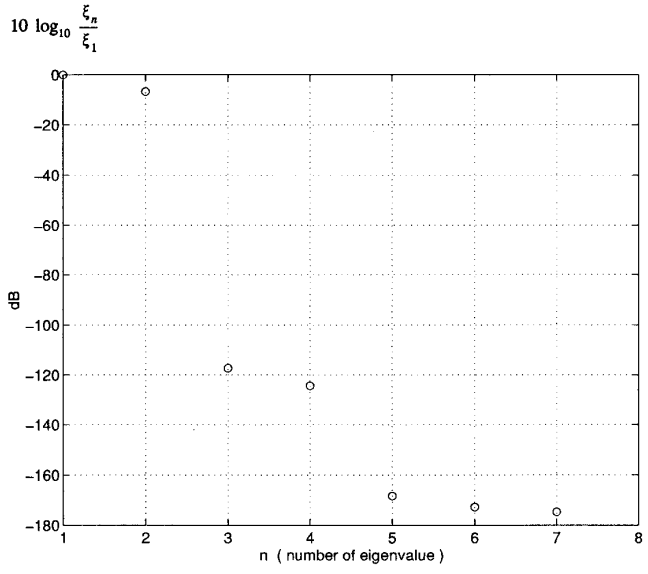


FIG. 6. Normalized magnitude of the eigenvalues of $Z_{fb}^{H} Z_{fb}$. The same input data as in Fig. 4, but $\theta_1 - \theta_2 = 178.2°$ (best case) and $L = 6$.

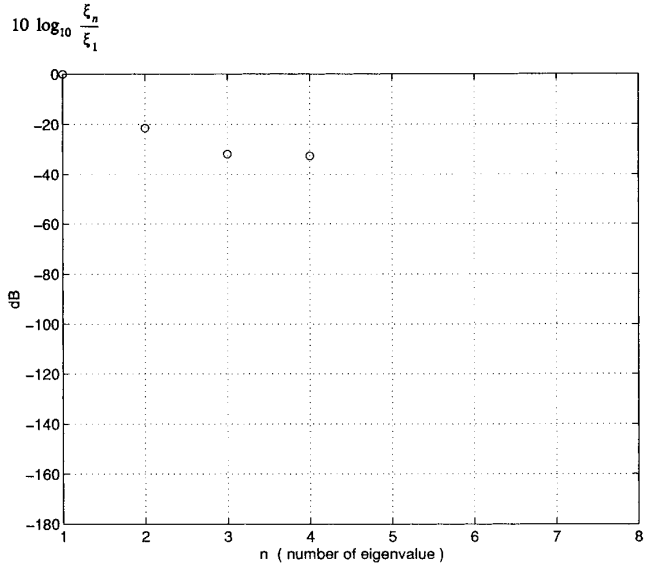


FIG. 8. Normalized magnitude of the eigenvalues of $Z_{fb}^{H} Z_{fb}$. The same input data as in Fig. 4, but SNR = 20 dB.

*4.3.4. TFBMPM for frequencies estimation in presence of noise.* In this section the number of frequency components, $K$, is assumed to be known and equal to 2.

Figures 12 and 13 show the TFBMPM performance as a function of SNR and $f_2 - f_1$. Figure 12 has been obtained for the worst case of $\theta_1 - \theta_2$ according to (4.3.2.3), while Fig. 13 corresponds to the best case estimation, (4.3.2.2). Note that the variance of $\hat{f}_1$ is referred to the CRB, which means that the (SNR) – ($f_2 - f_1$) plane represents the CRB. Both figures demonstrate that the TFBMPM works beyond a certain threshold of SNR.

Consequently, the threshold is an indicator of the estimation limits. For example, for the worst case, and for $f_2 - f_1 = 0.070$ Hz, the threshold is between 17 and 19 dB, as is shown in Fig. 12; therefore this is the SNR lower limit in order for the TFBMPM to provide reasonable results.

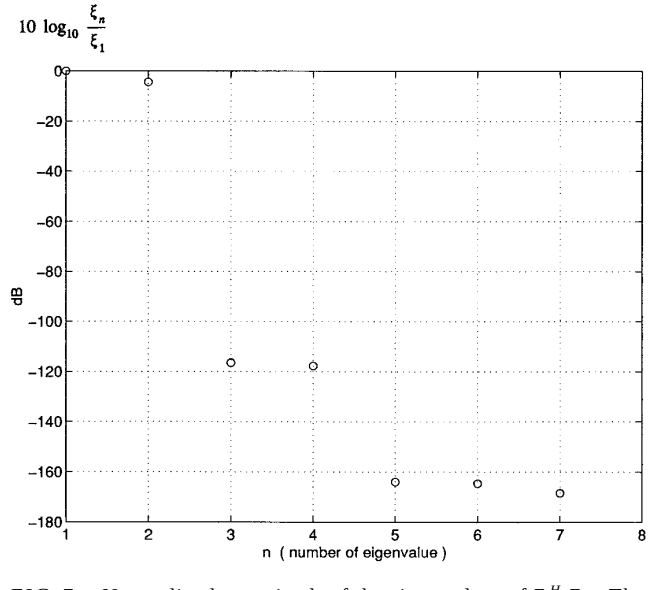


FIG. 7. Normalized magnitude of the eigenvalues of $Z_{fb}^{H} Z_{fb}$. The same input data as in Fig. 4, but $\theta_1 - \theta_2 = 23.4°$ (best case), $f_2 = 0.290$ Hz, and $L = 6$.

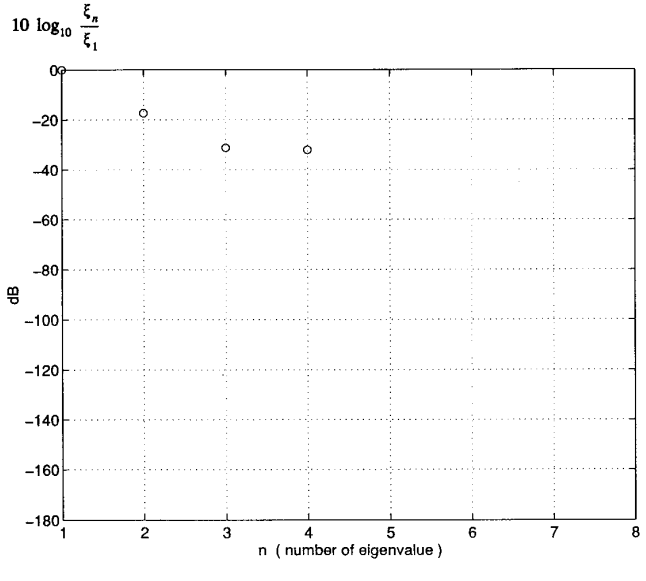


FIG. 9. Normalized magnitude of the eigenvalues of $Z_{fb}^{H} Z_{fb}$. The same input data as in Fig. 5, but SNR = 20 dB.

TABLE 2

Input Data Considered for Figs. 4 to 11

| Figure | SNR (dB) | $L$ | $f_2-f_1$ (Hz) | $\theta_1-\theta_2$ (°) |
|---|---|---|---|---|
| 4 | ∞ (noiseless) | 3 | 0.070 | 88.2 (worst case) |
| 5 | ∞ (noiseless) | 3 | 0.090 | 113.4 (worst case) |
| 6 | ∞ (noiseless) | 6 | 0.070 | 178.2 (best case) |
| 7 | ∞ (noiseless) | 6 | 0.090 | 23.4 (best case) |
| 8 | 20 | 3 | 0.070 | 88.2 (worst case) |
| 9 | 20 | 3 | 0.090 | 113.4 (worst case) |
| 10 | 20 | 6 | 0.070 | 178.2 (best case) |
| 11 | 20 | 6 | 0.090 | 23.4 (best case) |

For the best estimate, and $f_2 - f_1 = 0.070$ Hz, the lower limit is between 5 and 6 dB, as is shown in Fig. 13.

Figures 14 and 15 have been extracted from the data used in Figs. 2 and 3 and thus correspond to a SNR of 17 dB. Also 0.070 Hz is the designated value for $f_2 - f_1$ in Fig. 14 and 0.090 Hz is the value in Fig. 15.

In Fig. 14 the CRB is reached for all $\theta_1 - \theta_2$ except in the interval (70°, 105°), approximately, where the TFBMPM is not performing well. The reason can be found in Fig. 12, obtained for the worst case of $\theta_1 - \theta_2$, where one can see that for $f_2 - f_1 = 0.070$ Hz, a SNR of 17 dB is below the threshold and, by definition, the estimator ceases functioning. Nevertheless, the CRB is always reached in Fig. 15 because 17 dB is above the threshold for all $\theta_1 - \theta_2$ (for the worst case estimation the threshold for $f_2 - f_1 = 0.090$ Hz is between 13 and 14 dB, as is shown in Fig. 12).

## 5. THE FOURIER TRANSFORM ESTIMATOR

### 5.1. The Periodogram

The Fourier Transform Estimator (FTE) for frequency components estimation considered in this work is based on the classic periodogram. The estimates of the frequencies, $\hat{f}_m$ ($m = 1, \ldots, K$), will be the values of the variable $f$ (frequency) which maximize (local maxima) the periodogram, $\wp(f)$. The periodogram is an estimate of the power density spectrum and can be defined [14] as

$$\wp(f) = \frac{1}{N\Delta t} |Z(f)|^2, \qquad (5.1.1)$$

where $Z(f)$ is the Discrete-Time Fourier Transform (DTFT) of the noise samples,

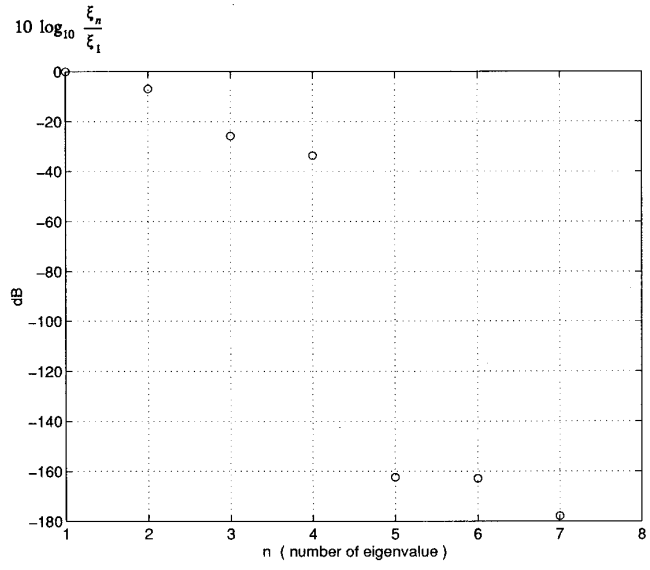


FIG. 10. Normalized magnitude of the eigenvalues of $Z_{fb}^H Z_{fb}$. The same input data as in Fig. 6, but SNR = 20 dB.

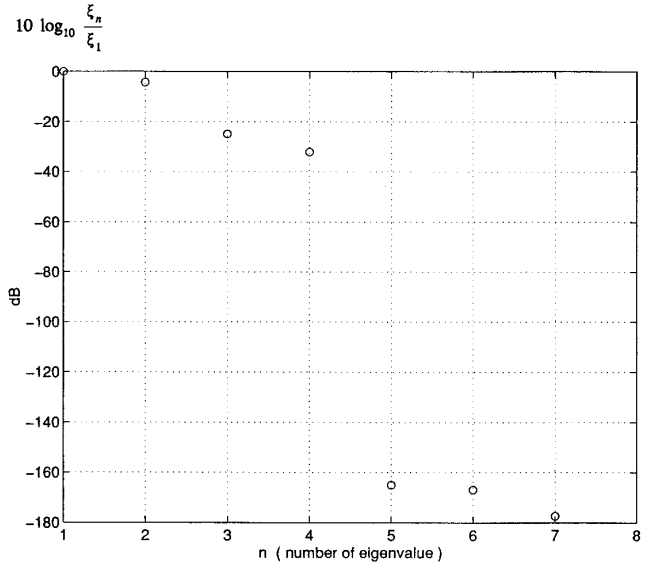


FIG. 11. Normalized magnitude of the eigenvalues of $Z_{fb}^H Z_{fb}$. The same input data as in Fig. 7, but SNR = 20 dB.

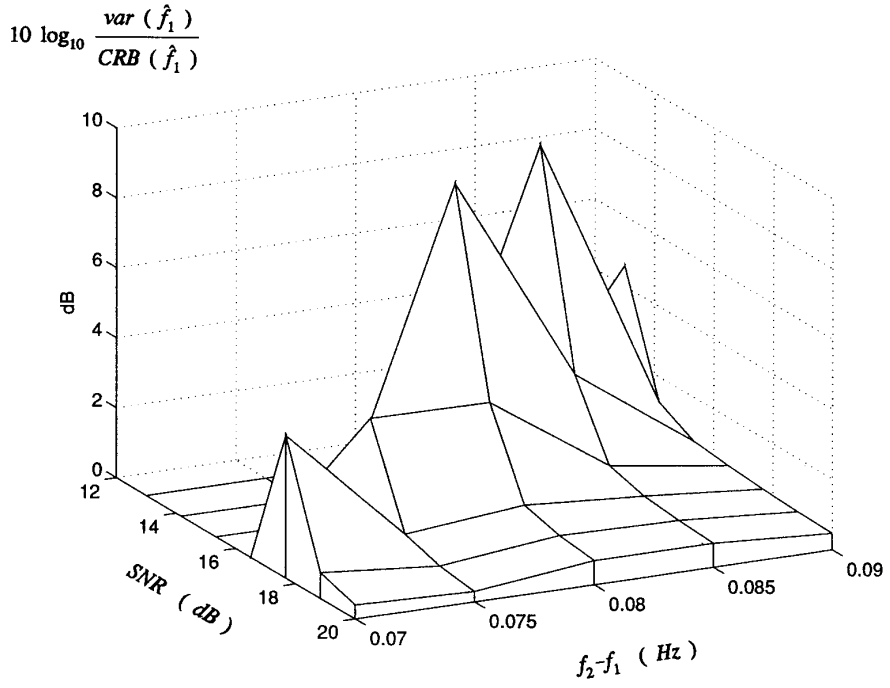


FIG. 12. Variance of $\hat{f}_1$ compared to the CRB for the worst case estimation. The peaks show the threshold of the TFBMPM.

$$Z(f) = \Delta t \sum_{i=0}^{N-1} z_i e^{-j2\pi f i \Delta t}, \; -\frac{1}{2\Delta t} \leqslant f \leqslant \frac{1}{2\Delta t}. \tag{5.1.2}$$

Figure 16 shows the normalized periodogram for the complex signal of Fig. 1. Note that the SNR assumed for this example is $\infty$ (noiseless samples). The two main peaks correspond to the two frequency components of the signal.

### 5.2. *Consequences of the Leakage Effect for Frequencies Estimation*

It is well known [15, pp. 136–144] that side lobes (see Fig. 16) appear in the DTFT of a finite length sequence, $z_i$ ($i = 0, \ldots, N-1$). This phenomenon, called leakage, becomes more evident when the frequencies move closer or when one frequency component is much stronger than the rest.

In order to mitigate the leakage effect, windows (weighting functions) are used. An observation interval, $N\Delta t$, is equivalent to a rectangular window, $h(i\Delta t)$, applied to the original signal, resulting in a finite set of samples, $z(i\Delta t)$:

$z_{\text{original}}(i\Delta t)$ defined for

$$i = -\infty, \ldots, -1, 0, 1, \ldots, +\infty \tag{5.2.1}$$

$$z(i\Delta t) = z_{\text{original}}(i\Delta t) \cdot h(i\Delta t), \quad i = 0, 1, \ldots, N-1 \tag{5.2.2}$$

$$h(i\Delta t) = \begin{cases} 1, & 0 \leqslant i\Delta t \leqslant (N-1)\Delta t \\ 0, & \text{otherwise.} \end{cases} \tag{5.2.3}$$

In terms of the DTFT the finite record is periodically extended, in the time domain, with period $N\Delta t$. If this period does not match the natural period of the signal, discontinuities appear at the boundaries of the record. These discontinuities [16] are the cause of the leakage. The function of a window is to reduce them. For this reason it is required that a window go to zero smoothly at its boundaries.

Even if an appropriate window can reduce the bias of the frequency estimate, the application of a window has a disadvantage as it decreases the spectral resolution. Consequently, one has to make a trade-off between the spectral resolution desired and the reduction of the side lobes. In any case, the spectral resolution, in Hz, is limited [15, pp. 46–49] to the reciprocal of the observation time, $(N\Delta t)^{-1}$. Therefore, frequency components separated by a distance less than $(N\Delta t)^{-1}$ will not be distinguished by the FTE, that is, the case of simulations carried out in Section 4.3, where

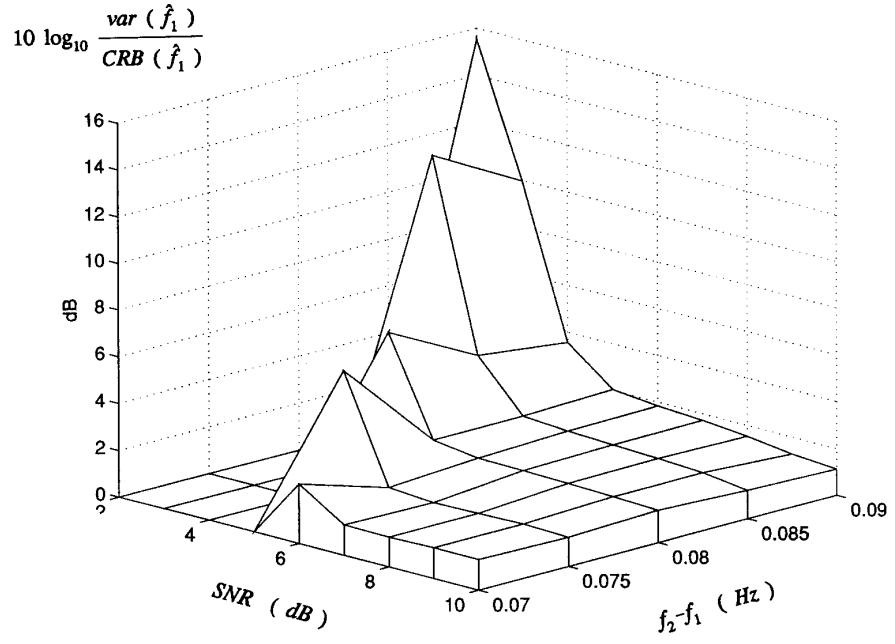


FIG. 13. Variance of $\hat{f}_1$ compared to the CRB for the best case estimation. The peaks show the threshold of the TFBMPM.

$(N\Delta t)^{-1}$ is 0.125 Hz and the maximum $\Delta f$ studied is 0.090 Hz and, in consequence, the FTE does not work under those conditions.

Three windows have been considered in this work:

Rectangular window

$$h_i = \begin{cases} 1, & 0 \leqslant i \leqslant N-1 \\ 0, & \text{otherwise;} \end{cases} \tag{5.2.4}$$

Standard window [11]

$$h_i = \begin{cases} \dfrac{1}{3}\displaystyle\sum_{k=0}^{3} a_k \cos\left(\frac{2\pi i k}{N}\right), & 0 \leqslant i \leqslant N-1 \\ 0, & \text{otherwise;} \end{cases} \tag{5.2.5}$$

with $a_0 = 1$, $a_1 = -1.43596$, $a_2 = 0.497536$, $a_3 = -0.061576$.

Kaiser window [17, p. 232]

$$h_i = \begin{cases} \dfrac{I_0[\beta \cdot \sqrt{1-((i-N/2)/N/2)^2}]}{I_0[\beta]}, & 0 \leqslant i \leqslant N-1 \\ 0, & \text{otherwise;} \end{cases} \tag{5.2.6}$$

here $I_0[\cdot]$ is the modified Bessel function of the first kind and order zero and $\beta$ is a parameter, and in this work it has been chosen according to Table 3.

In Figs. 17 and 18 the windows are shown in both time and frequency domains. The number of samples has been taken as 12 and the sampling period is 0.25 ms. The main difference among these windows is the reduction in the side lobes. The Standard window achieves the largest reduction of the bias, but it does so at the expense of broadening the main lobe, which results in a loss of spectral resolution.

The window in the time domain is applied by weighting the input samples, $z_i$, with the window coefficients, $h_i$, by modifying Eq. (5.1.2) in the following way:

$$Z(f) = \Delta t \sum_{i=0}^{N-1} z_i h_i e^{-j2\pi f i \Delta t}, \; -\frac{1}{2\Delta t} \leqslant f \leqslant \frac{1}{2\Delta t}. \tag{5.2.7}$$

Eq. (5.2.7) is simply the DTFT of the weighted samples, $z_i h_i$, and it will be used, jointly with (5.1.1), to estimate the frequency components.

### *5.3. Comparison between the FTE and the TFBMPM*

The frequency component estimation using the Fourier Transform has been widely studied by Rife and Boorstyn in [11]. Figure 19 provides the comparison between various windows and the TFBMPM.

The input data for Fig. 19 are given by Fig. 1, and the SNR, which is defined in (4.3.1.3), varies

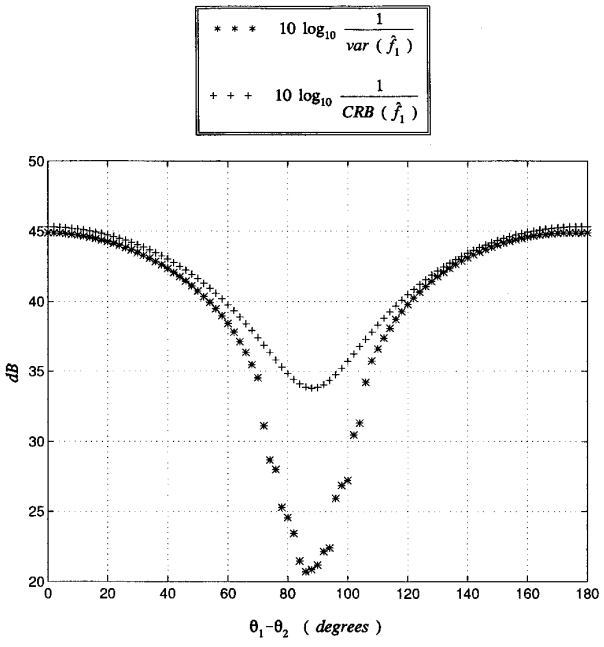


FIG. 14. Comparison between the inverse of the variance and the CRB for the first frequency estimate. $f_2 - f_1 = 0.070$ Hz and SNR = 17 dB. The TFBMPM produces inaccurate results in $\theta_1 - \theta_2 \in (70°, 105°)$ because the SNR is below the threshold.

between 0 and 40 dB. The values corresponding to the CRB (dark squares in Fig. 19) have been computed by the square root of the corresponding diagonal term in the inverse of the Fisher Information Matrix (4.2.20) and the pencil parameter, $L$, for the TFBMPM has been taken as 22. The statistical magnitude represented in Fig. 19 is the root mean squared error (rmse), defined as

$$\text{rmse}(\hat{f}_1) = \sqrt{E[(\hat{f}_1 - f_1)^2]}, \qquad (5.3.1)$$

where $E[\cdot]$ means expected value, $\hat{f}_1$ is the parameter being estimated, and $f_1$ is the true value of the parameter. The rmse is related to the variance through the bias, i.e.,

$$\text{rmse}^2(\hat{f}_1) = \text{bias}^2(\hat{f}_1) + \text{var}(\hat{f}_1), \qquad (5.3.2)$$

and, evidently, for unbiased estimators the rmse becomes the square root of the variance. The rmse was computed using 200 trials for each algorithm.

From Fig. 19 one can see that the TFBMPM is performing better than the FTE in all the SNR range. On the other hand, and in spite of the smaller bias presented by the Standard window (see Fig. 20), the Kaiser window provides better results than the Standard window for SNR below 30 dB. The reason for this is that the Standard window achieves a reduction of the bias but at the expense of increasing the variance of the estimate.

The bias shown in Fig. 20 was computed according to

$$\text{bias}(\hat{f}_1) = E[\hat{f}_1] - f_1, \qquad (5.3.3)$$

and one can see that for SNR below 10 dB the FTE with the Standard window offers less bias than the TFBMPM. Nevertheless, the rmse obtained with the TFBMPM is less than the one computed using the Standard window as seen in Fig. 19. This is because the Standard window reduces the bias but at the same time increases the variance. On the other hand, the use of the Rectangular window makes a FTE biased even for high SNR.

In Fig. 21 the behavior of the estimator as the number of samples increases is shown. The input data are the same as in Fig. 19, but a $\Delta\theta$ of worst case was taken for each $N$, and SNR = 0 dB. The FTE uses the Kaiser window for this simulation and it can be seen that for long data record the FTE reaches the CRB.

Figure 22 shows a comparative study of the rmse as a function of the difference of frequencies $f_1 - f_2$ for two components of equal power when the SNR is 20 dB. As in Fig. 19 the sampling period is 0.25 ms but the number of samples has been drastically

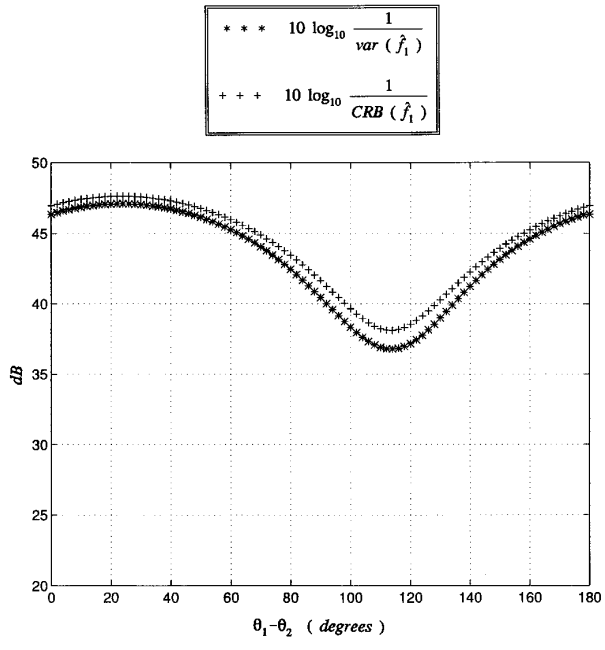


FIG. 15. Comparison between the inverse of the variance and the CRB for the first DOA estimate. $f_2 - f_1 = 0.090$ Hz and SNR = 17 dB. The TFBMPM reaches the CRB for all $\theta_1 - \theta_2$ because the SNR is above the threshold.

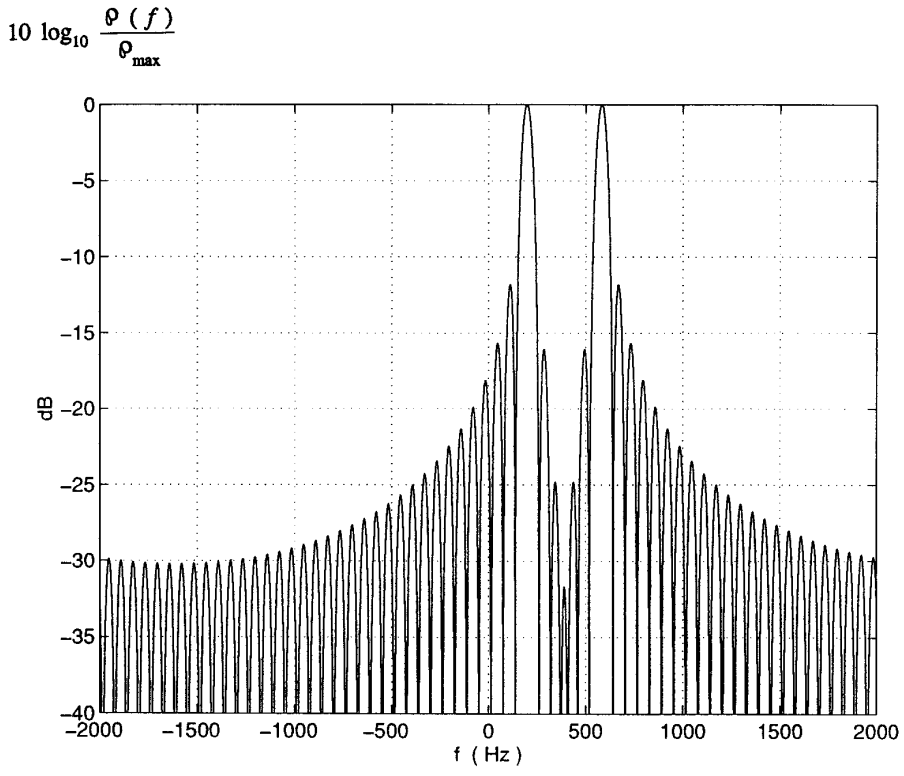


FIG. 16. Normalized periodogram of the undamped cisoid of Fig. 1. A Rectangular window was used to weight the samples in the time domain.

reduced from 64 to 12 samples. The pencil parameter for the TFBMPM is $L = 7$, $f_2$ is 200 Hz, and $\Delta\theta$ (worst case) is assumed according to (5.3.2.3). Two main conclusions can be drawn from Fig. 22; on the one hand the FTE does not work for $\Delta f$ below 460 Hz ($(N\Delta t)^{-1}$ is 333 Hz) while TFBMPM still performs well up to 180 Hz and, on the other hand, the TFBMPM performs better than the FTE even when FTE works, i.e., for $\Delta f$ greater than 460 Hz.

In Fig. 23 the accuracy of the estimators depending on the number of samples, $N$, is shown. A SNR of 15 dB for two frequency components of equal power at, respectively, 1300 and 1000 Hz was considered. Also a $\Delta t$ of 0.25 ms and a $\Delta\theta$ of worst case for each $N$ were taken. Similar conclusions to the ones for Fig. 22 can be derived.

TABLE 3

$\beta$ Values for the Kaiser Window

| Figure | $\beta$ Value |
|---|---|
| 17, 18, 19, 20, 21, 22 | 6 |
| 23 | 5.5 |
| 24, 25, 26, 27 | 5 |

The last simulation included in this paper is shown in Figs. 24 to 28. While in the previous simulations the two frequency components had the same power, in Figs. 24 to 28, the first frequency component has 10 times more power than the second one,

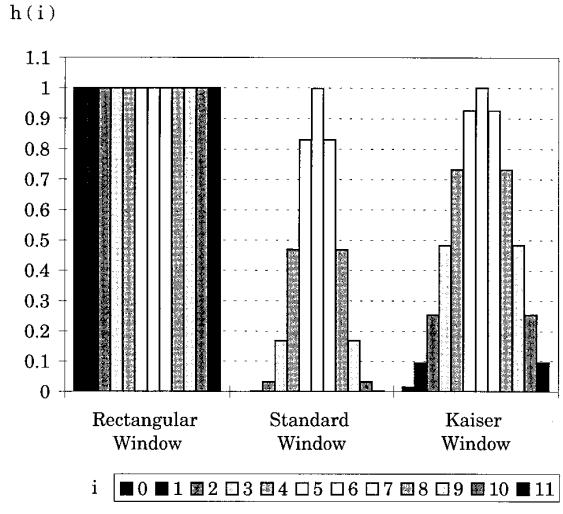


FIG. 17. The three windows used in this work for the Fourier Transform Estimator (FTE). The graph shows 12 samples for each of them in the time domain.

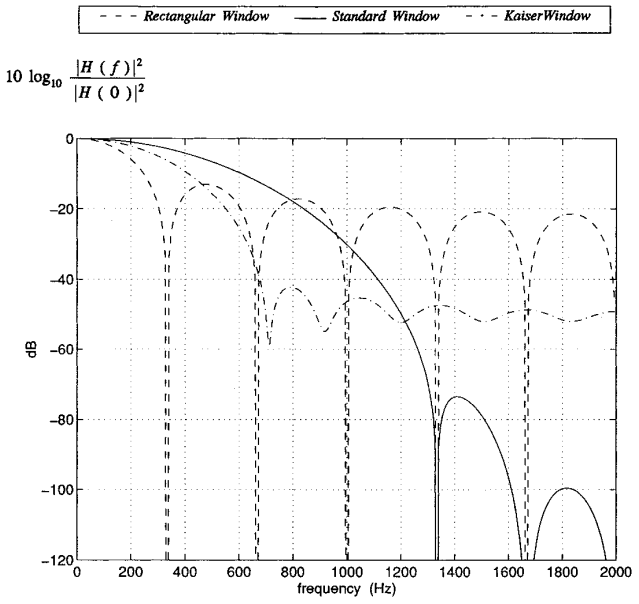


FIG. 18. Comparative spectrum of the windows. The Discrete Time Fourier Transform (DTFT) was used to obtain $H(f)$.

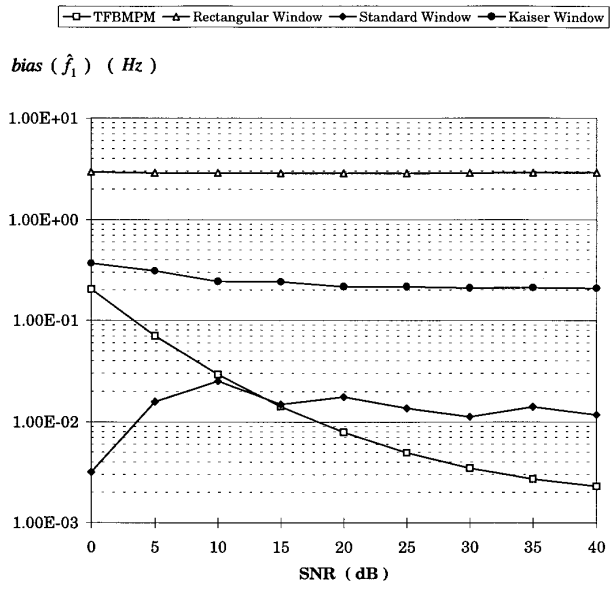


FIG. 20. Bias for the estimate of Fig. 19. In spite of the fact that the Standard window offers less bias than the TFBMPM for SNR below 10 dB, its rmse performance is worse because the Standard window increases the variance.

i.e., $|A_1|^2 = 10\ |A_2|^2$, which supposes that $SNR_1$ (dB) = 10 dB + $SNR_2$ (dB). On the other hand, 0.25 ms for the sampling period and 12 samples characterize the observation interval. The pencil parameter used in the TFBMPM is 6, $f_2$ = 400 Hz, $SNR_2$ = 10 dB, and $\Delta\theta$ of worst case for each $\Delta f$ is chosen. From Figs. 24 and 25 one can see the better performance of the TFBMPM for both $\hat{f}_1$ and $\hat{f}_2$ estimates and also a larger spectral resolution for this estimator. At this point it is important to indicate that the

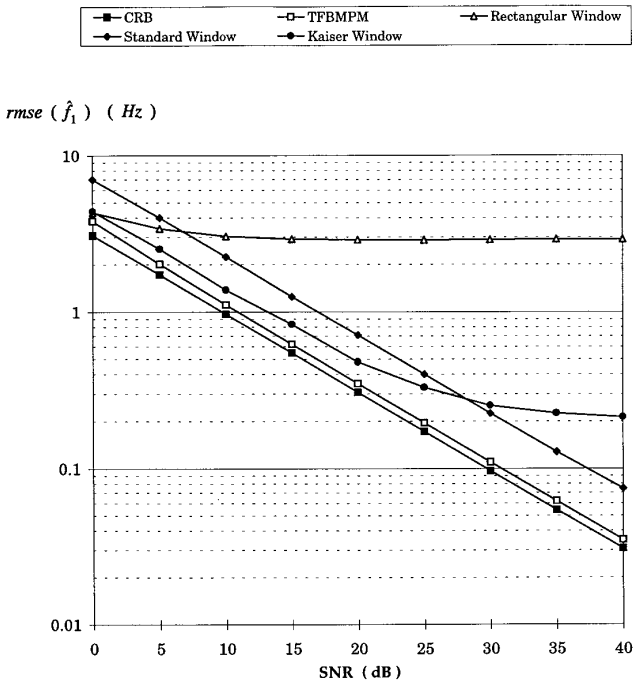


FIG. 19. A first comparison between the TFBMPM and the FTE. Several SNR were considered for the signal of Fig. 1. A better performance of the TFBMPM is observed in the entire SNR range under study.

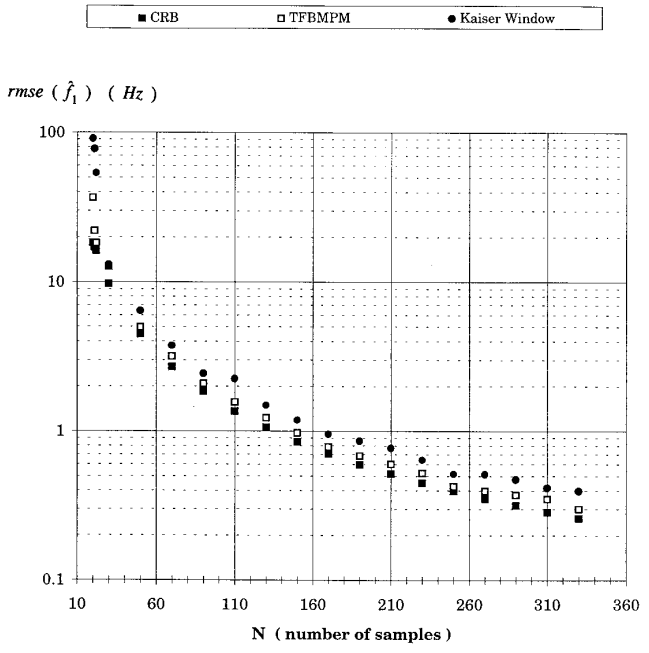


FIG. 21. The signal of Fig. 1 was contaminated with a SNR = 0 dB. For long data records the FTE reaches the CRB.

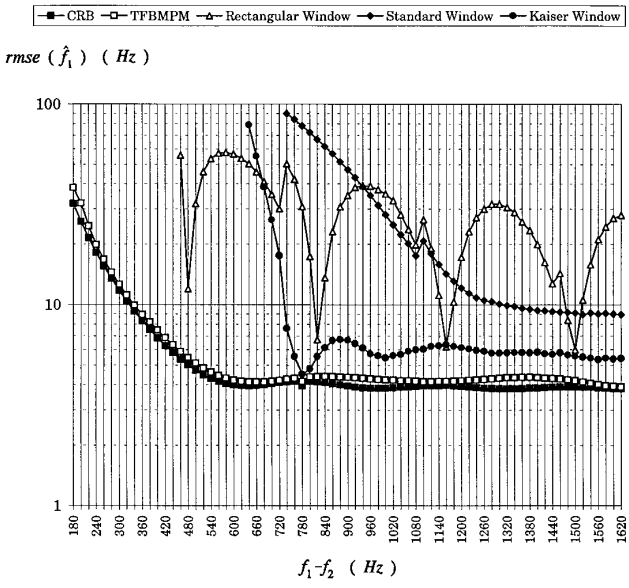


FIG. 22. The signal was built with two components of equal power and SNR = 20 dB. The observation interval is characterized by 12 samples and $\Delta t$ = 0.25 ms. Better performance and higher spectral resolution are observed for the TFBMPM.

criterion applied to consider whether an estimate is valid, when the FTE is used, has consisted of being able to distinguish the two frequency components. This idea is reflected in Fig. 26, where the Kaiser window is used for the FTE, $f_1$ is 1400 Hz, $f_2$ is 400 Hz, and $\Delta\theta = 45°$. The opposite case is shown in Fig.

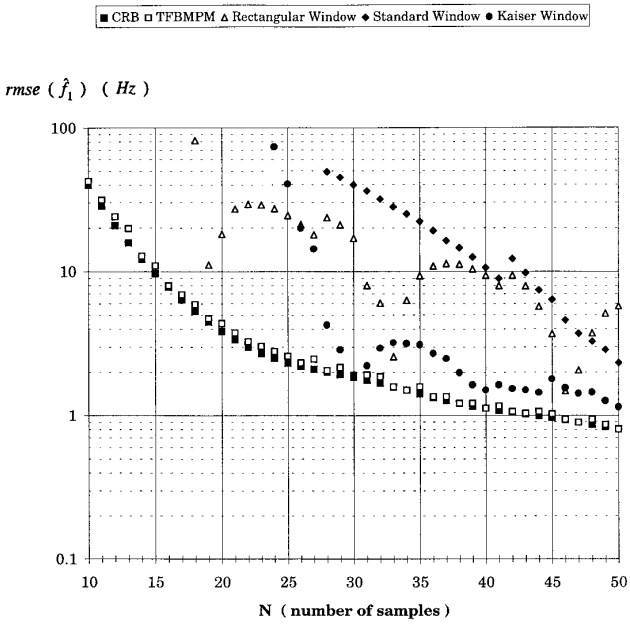


FIG. 23. A dual behavior to the one of Fig. 21 is derived. A SNR of 15 dB was chosen for two components of equal power and 300 Hz apart.

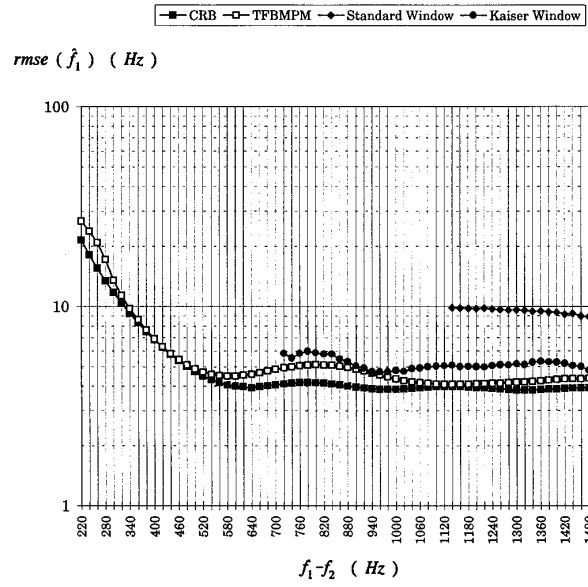


FIG. 24. rmse of the first estimate, $\hat{f}_1$, for a signal composed by two frequency components. The first component has 10 times more power than the second one. $SNR_2$ = 10 dB.

27, where the main lobe, centered in 1000 Hz ($f_1$), is masking the lobe corresponding to the second frequency component, $f_2$, at 400 Hz. The Rectangular window was not considered in this simulation because, for some frequencies, the smaller frequency component, $f_2$, was hidden for side lobes, as is shown in Fig. 28. The two frequency components of the signal for that example are $f_1$ = 1860 Hz and $f_2$ = 400 Hz, and $\Delta\theta = 177.3°$.

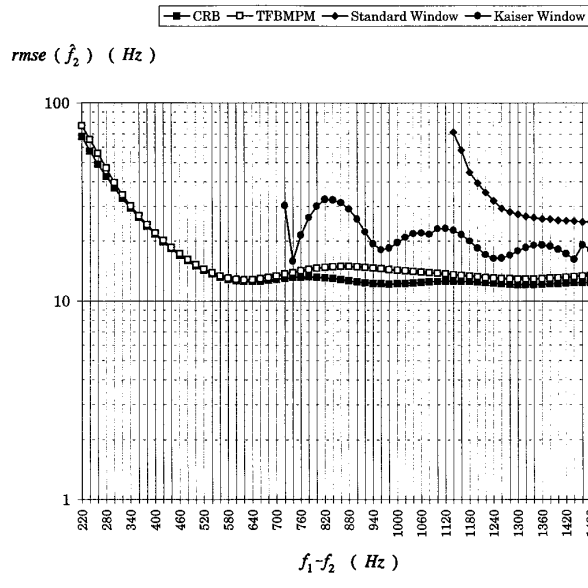


FIG. 25. The same input data as in Fig. 23 but the estimate evaluated is $\hat{f}_2$.

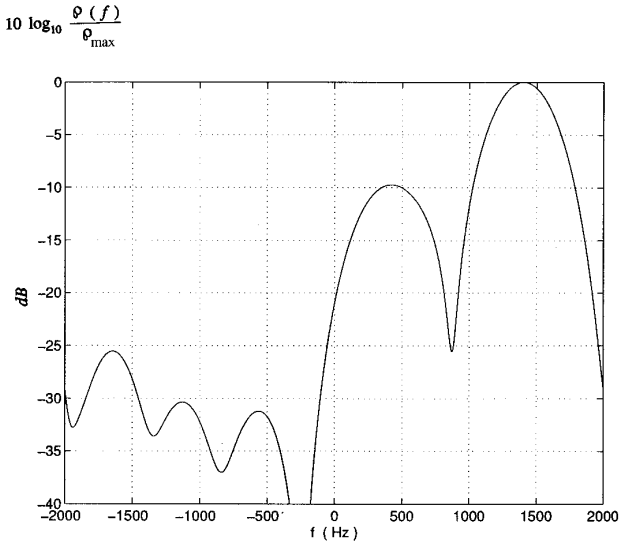


FIG. 26. The two main lobes centered, respectively, at 1400 and 400 Hz, can be distinguished from each other. The first main lobe has 10 times more power than the second one.

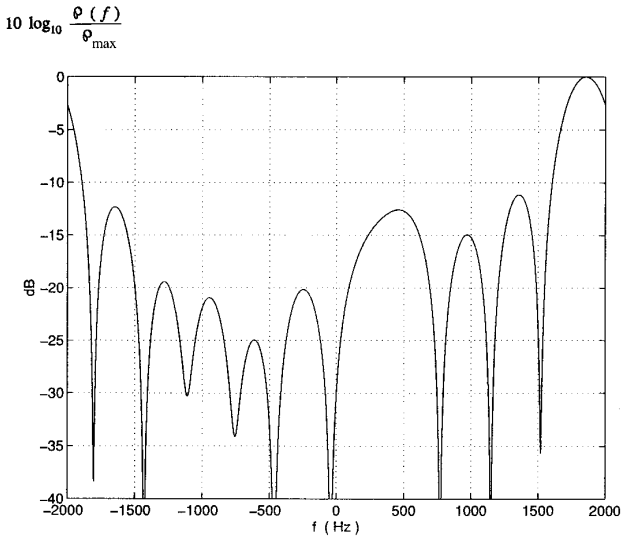


FIG. 28. For some difference of frequencies, the second main lobe is hidden by side lobes when the Rectangular window is applied and, consequently, the FTE will not work.

## 6. CONCLUSIONS

The objective of this paper has been to present the TFBMPM and the Fourier Transform Technique for the estimation of undamped cisoids in white Gaussian noise. The accuracy of TFBMPM has been brought out in the presence of noise and its variance compared to that of the Cramer–Rao Bound.

It has been shown that applying windowing in the Fourier Transform provides unbiased estimates at the expense of spectral resolution. The Rectangular, Standard, and Kaiser windows have been chosen as the representatives for numerical simulation. It has been shown that when TFBMPM works beyond a certain threshold of SNR, it provides better variance estimates than the Fourier techniques, although the bias may be large. However, the root mean squared error is less for the TFBMPM than for the Fourier Techniques with various windows.

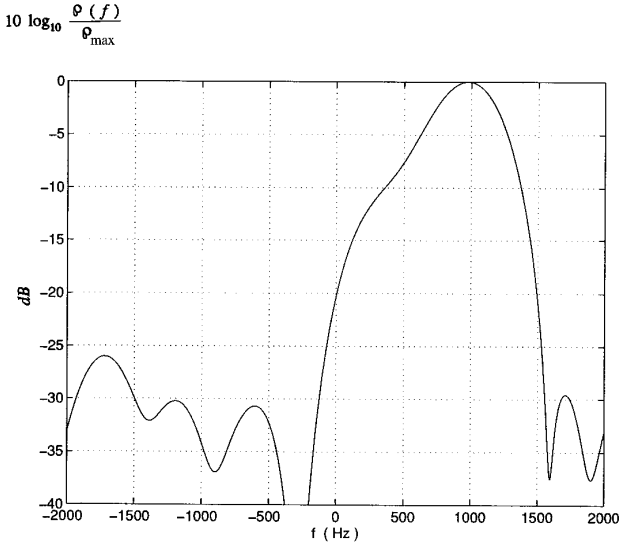


FIG. 27. The first main lobe, at 1000 Hz, is masking the second main lobe centered at 400 Hz.

## REFERENCES


1. Hua, Y., and Sarkar, T. K. Matrix pencil method for estimating parameters of exponentially damped/undamped sinusoids in noise. *IEEE Trans. Acoust. Speech Signal Process.* 38, No. 5 (May 1990), 814–824.
2. Hua, Y. *On techniques for estimating parameters of exponentially damped / undamped sinusoids in noise.* Ph.D. dissertation, Syracuse University, New York, Aug. 1988.
3. Golub, G. H., and Van Loan, C. F. *Matrix Computations.* The John Hopkins Univ. Press, Baltimore, 1985.
4. Hua, Y., and Sarkar, T. K. Matrix pencil method and its performance. In *Proc. ICASSP-88, New York,* 1988, pp. 2476–2479.
5. Johnson, D. H., and Dudgeon, D. E. *Array Signal Processing: Concepts and Techniques.* Prentice Hall, Englewood Cliffs, NJ, 1994.
6. Cramer, H. *Mathematical Methods of Statistics.* Princeton Univ. Press, Princeton, NJ, 1966.
7. Slepian, D. Estimation of signal parameters in the presence of noise. *IRE Trans. Inform. Theory* PGIT-3 (March 1954), 68–89.
8. Brennan, L. E. Angular accuracy of phased array radar. *IRE Trans. Antennas Propagation* AP-9 (May 1961), 268–275.

9. Hua, Y., and Sarkar, T. K. A. Note on the Cramer–Rao bound for 2-d direction finding based on 2-d array. *IEEE Trans. Signal Process.* 39, No. 5 (May 1991), 1215–1218.
10. Shanmugan, K. S., and Breipohl, A. M. *Random Signals: Detection, Estimation and Data Analysis.* Wiley, New York, 1988.
11. Rife, D. C., and Boorstyn, R. R. Multiple tone parameter estimation from discrete-time observations. *Bell System Tech. J.* 55, No. 9 (Nov. 1976), 1389–1410.
12. IMSL, INC. IMSL Library. *Problem-Solving Software Systems for Mathematical and Statistical FORTRAN Programming.* Nov. 1984.
13. Sarkar, T. K., Hu, F., Hua, Y., and Wicks, M. A real-time signal processing technique for approximating a function by a sum of complex exponentials utilizing the matrix-pencil approach. *Digital Signal Process.* 4, (1994), 127–140.
14. Kay, S. M., and Marple, S. L., Jr. Spectrum analysis—A modern perspective. *Proc. IEEE* 69, No. 11 (Nov. 1981), 1380–1419.
15. Marple, S. L., Jr. *Digital Spectral Analysis with Applications.* Prentice Hall, Englewood Cliffs, NJ, 1987.
16. Harris, F. J. On the use of windows for harmonic analysis with the discrete Fourier transform. *Proc. IEEE* 66, No. 1 (Jan 1978), 51–83.
17. Kuo, F. F., and Kaiser, J. F. *System Analysis by Digital Computer.* Wiley, New York, 1966.

---

JOSE ENRIQUE FERNANDEZ DEL RIO was born in Santoña, Cantabria, Spain, on December 28, 1965. He graduated in 1992 as the valedictorian of his class with a B.S. degree in Physics–Electronics from the University of Cantabria, Santander, Spain. In 1994 he received the M.S. degree in Electrical Engineering, also from the University of Cantabria. For two years he was a member of a research team of the University of Cantabria, where he worked on POWERCAD, a project which is part of ESPRIT, one of the research programs sponsored by the European Community. His task consisted in modeling the inductive coupling and the radiated noise in switched mode power Supplies. From 1994 to 1995 he was a visiting scholar in the Department of Electrical and Computer Engineering at Syracuse University, Syracuse, NY. He came to Syracuse with a fellowship from the Marcelino Botín Foundation (Santander, Spain). He is currently working toward his Ph.D. degree in the University of Cantabria, studying different topics related to applied electromagnetics. His research interests include signal processing and electromagnetic compatibility.

TAPAN KUMAR SARKAR was born in Calcutta, India, on August 2, 1948. He received the B. Tech. degree from the Indian Institute of Technology, Kharagpur, India, in 1969, the M.Sc.E. degree from the University of New Brunswick, Fredericton, Canada, in 1971, and the M.S. and Ph.D. degrees from Syracuse University, Syracuse, NY in 1975. From 1975 to 1976 he was with the TACO Division of the General Instruments Corporation. He was with the Rochester Institute of Technology, Rochester, NY, from 1976 to 1985. He was a Research Fellow at the Gordon McKay Laboratory, Harvard University, Cambridge, MA, from 1977 to 1978. He founded OHRN Enterprises in 1985, which has been engaged in signal processing research and development, with several governmental and industrial organizations. He is also a professor in the Department of Electrical and Computer Engineering, Syracuse University, Syracuse, NY. His current research interests deal with adaptive polarization processing and numerical solutions of operator equations arising in electromagnetics and signal processing with application to radar system design. He obtained one of the "best solution" awards in May 1977 at the Rome Air Development Center (RADC) Spectral Estimation Workshop. He has authored or coauthored more than 154 journal articles and conference papers and has written chapters in eight books. Dr. Sarkar is a registered professional engineer in the State of New York. He received the Best Paper Award of the *IEEE Transactions on Electromagnetic Compatibility* in 1979. He was an Associate Editor for feature articles of the *IEEE Antennas and Propagation Society Newsletter,* the Technical Program Chairman for the 1988 IEEE Antennas and Propagation Society International Symposium and URSI Radio Science Meeting, and an Associate Editor of the *IEEE Transactions of Electromagnetic Compatibility.* He was an Associate Editor of the *Journal of Electromagnetic Waves and Applications* and on the editorial board of the *International Journal of Microwave and Millimeter Wave Computer Aided Engineering.* He has been appointed U.S. Research Council Representative to many URSI General Assemblies. He is the Chairman of the Intercommission Working Group of International URSI on Time Domain Metrology. Dr. Sarkar is a member of Sigma Xi and International Union of Radio Science Commissions A and B.